Lab on a Chip

PAPER

View Article Online
View Journal

Cite this: DOI: 10.1039/d6lc00190d

Independent parallel production of tunable blood clot analogues in hourglass-profiled circular PDMS fluidic channels

Chun-Hsin Hsu,†[a] To-Wen Chen,†[a] Wei-Jen Soong [a] and Chihchen Chen *[ab]

Received 27th February 2026,
Accepted 21st April 2026

DOI: 10.1039/d6lc00190d

rsc.li/loc

Rapid removal of occluding blood clots, whether by intravenous thrombolysis or endovascular thrombectomy, can be life-saving. Yet recanalization is not always successful, and the determinants remain incompletely understood. Thrombi exhibit heterogeneous compositions, while clinical samples and animal models are costly, variable, and often lack reproducibility. To address these challenges, we present a blood clot analogue production system capable of generating tunable clot analogues in parallel under precisely regulated flow and calcium ion conditions. The platform integrates one or multiple pressure-controlled fluidic loops operating independently with a single pump and multiple hourglass-profiled circular devices fabricated from poly(dimethylsiloxane) (PDMS), a gas-permeable material that replicates vascular occlusion hemodynamics. Using this system, clot analogues measuring approximately 0.8 cm to over 2.5 cm in length were generated, displaying heterogeneous upstream–constriction–downstream architectures in which the red blood cell (RBC)–fibrin fraction could be tuned between 23% and 76%, closely mirroring clinical thrombi. The composition was modulated through recalcification under various $CaCl_2$ concentrations (1.8–16.5 mM) and shear rates (10^4–10^6 s^{-1}). At higher Ca^{2+} levels (≥6.6 mM), compact RBC–fibrin-dominated clots formed rapidly (<10 minutes), displaying laminar "Zahn line" structures. In contrast, lower Ca^{2+} conditions (1.8–2.3 mM) delayed occlusion (>40 minutes) and yielded diffuse neutrophil extracellular trap (NET)-platelet networks. The system operates stably for >1000 minutes with recirculating blood, ensuring reproducibility and cost-effectiveness while reducing reliance on animal thrombosis models in accordance with the 3R (replacement, reduction, and refinement) principles. Collectively, this platform provides a controllable, ethically responsible, and physiologically relevant model for thrombogenesis and thrombectomy research.

1. Introduction

Ischemic heart disease has remained the leading cause of mortality worldwide since 1990, according to Global Burden of Disease studies.[1–3] Thrombus formation and subsequent embolization are central pathological processes underlying ischemic heart disease, stroke, and pulmonary embolism, underscoring the urgent need for deeper mechanistic insights and therapeutic innovation.[4,5] Endovascular thrombectomy has emerged as a highly effective treatment for large-vessel occlusion strokes, offering substantial clinical benefit regardless of prior or concomitant pharmacological thrombolysis.[6–8] Despite its success, outcomes remain variable, and recent studies suggest that thrombus composition plays a critical role in determining procedural efficacy. RBC-rich thrombi are associated with higher rates of successful recanalization and shorter procedure times, whereas platelet-rich thrombi, characterized by dense fibrin networks interspersed with leukocytes and extracellular DNA, may contribute to therapeutic resistance.[9–12] These observations highlight the importance of understanding thrombus heterogeneity and its impact on treatment response, with peri-interventional compositional assessment offering potential prognostic value and guidance for therapeutic optimization.

Nevertheless, the direct incorporation of thrombus composition into clinical decision-making remains poorly defined.[13,14] Addressing this gap requires the development of a stable and reproducible *in vitro* platform capable of generating thrombi for systematic investigation and translational applications. Given that thrombectomy outcomes are strongly influenced by thrombus composition, the creation of physiologically relevant human clot analogues that recapitulate the heterogeneous phenotypes observed in patients, and their

---

[a] *Institute of NanoEngineering and Microsystems, National Tsing Hua University, Hsinchu 300044, Taiwan. E-mail: chihchen@mx.nthu.edu.tw*
[b] *Department of Power Mechanical Engineering, National Tsing Hua University, Hsinchu 300044, Taiwan*

† These authors contributed equally to this work.

validation within controlled *in vitro* thrombectomy platforms, represents a critical step toward standardizing device efficacy comparisons and refining interventional strategies. We reviewed clot formation methods, as detailed below and summarized in Table S1.

Previous attempts to reproduce clinically relevant thrombi *in vitro* have typically relied on combining red blood cells, platelets, and plasma under static or rotational conditions. However, histological analyses and mechanical tensile testing revealed notable deviations from native thrombi, underscoring the need for improved models that more faithfully capture the structural and compositional complexity of patient-derived specimens.[12,15] Other approaches have employed extracorporeal circulation systems, in which whole blood was perfused through closed-loop circuits incorporating glass segments with stenotic constrictions to mimic atherosclerotic narrowing. While these systems induced high shear stress, the intrinsic thrombogenicity of glass tubing confounded interpretation, making it difficult to discern whether thrombus formation was driven primarily by shear forces or by the substrate itself.[16]

These limitations highlight the urgent need for a reproducible *in vitro* platform capable of generating clot analogues under physiologically relevant hemodynamic conditions, thereby enabling clinically translatable models for systematic investigation and establishing a standardized framework for evaluating thrombectomy devices.

Dozens of microfluidic devices have been engineered to study hemostasis, with PDMS widely adopted for its ease of fabrication, versatility, biocompatibility, gas permeability, optical transparency, and elastomeric flexibility.[17–19] PDMS-based microfluidic systems have advanced experimental thrombosis research by allowing precise control of geometry and shear stress under physiological flow conditions. For example, Tovar-Lopez *et al.* demonstrated that PDMS microchannels could quantitatively capture platelet deposition and fibrin formation kinetics under controlled shear rates, establishing one of the first standardized "thrombosis-on-a-chip" assays.[20] Ramaswamy *et al.* later adapted PDMS microfluidics for point-of-care coagulation testing, enabling activated partial thromboplastin time (aPTT) measurements directly from whole blood.[21] Building on these frameworks, Berry *et al.* developed an "occlusive thrombosis-on-a-chip" for real-time visualization of platelet and fibrin dynamics under physiological flow, facilitating drug evaluation.[22] Endothelial cell-coated channels have also been devised to study compression injury,[23] though their rectangular cross-sections introduced flow distribution artifacts, particularly at corners where shear rates and leakage flows are most sensitive.[24,25]

In this study, we address the need for consistent blood clot analogues by employing hourglass-profiled circular PDMS fluidic devices. Multiple devices can be operated in parallel with a single pump using one or more blood batches. Clot formation is monitored in real time using microscopic imaging and flow-rate sensors. The hourglass profile enables shear-rate transitions from ~10^4 s^{-1} at the inlet to >10^6 s^{-1} at the constriction and back to 10^4 s^{-1} downstream. Beyond flow control, varying calcium chloride ($CaCl_2$) concentrations allow precise modulation of clot phenotype to simulate thrombus and embolus formation (Fig. 1). This combination of tunable shear and ionic environments provides a unified microfluidic platform for reproducing and comparing physiologically distinct thrombus types *in vitro*. Furthermore, elongated thrombi generated in the PDMS fluidic channel can be readily retrieved for downstream analysis, facilitating studies on mechanical thrombectomy while adhering to the principles of replacement, reduction, and refinement (3Rs).[26] This approach reduces reliance on animal models and offers a reproducible, ethically responsible platform for translational thrombosis and thrombectomy research.

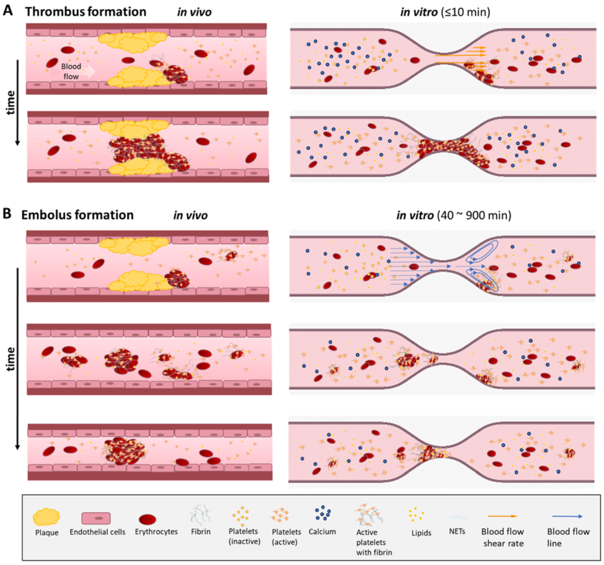

Fig. 1 Comparison between the physiological *in vivo* vascular environment and the *in vitro* hourglass-profiled circular fluidic channel. *In vivo*, elevated shear rates at stenotic regions promote platelet activation and aggregation, while reduced shear rates downstream support thrombus growth and stabilization. The hourglass-profiled circular fluidic channel replicates this hemodynamic transition, enabling controlled blood clot analogue formation under defined flow and ionic conditions. A) High calcium chloride ($CaCl_2$) concentrations in circulating blood induce the rapid formation of thrombus-like, RBC-fibrin-rich clot analogues. B) Low $CaCl_2$ concentrations favor the formation of embolus-like clot analogues enriched in neutrophil extracellular traps (NETs), platelets, and fibrin.

2. Experimental

2.1 Materials and equipment

Fluidic channels were fabricated from poly(dimethylsiloxane) (PDMS; Sylgard 184, Dow Corning, USA) using polymethyl methacrylate (PMMA; Kunchuan, Taiwan) master molds precision-milled with a computer numerical control (CNC) system (EGX-400, Roland DG, Japan) to define the three-dimensional channel geometry.

The experimental setup included a roller pump (C9ES-DG600LNE, DGS, Taiwan), flow-rate sensors (FD-XS8, Keyence, Japan), digital microscope imaging modules (TM4K, TOMLOV, China; UM20, Vitiny, Taiwan), adjustable-height platforms, and a microplate shaker (MX-M, DLAB, China).

Fresh porcine whole blood was obtained from the Agricultural Technology Research Institute (ATRI, Taiwan) and used on the day of collection. Samples were stored in citrate phosphate dextrose adenine-1 (CPDA-1) anticoagulant blood bags (JMS, Taiwan) until use.

Calcium chloride ($CaCl_2$; SI-C5670, Sigma-Aldrich, USA), phosphate-buffered saline (PBS, 1×; 10010023, Gibco, USA), and 4% paraformaldehyde (PFA; J60401, Alfa Aesar, USA) were used in the experiments. For histological analysis, hematoxylin (TA01MH, BIOTnA Biotech, Taiwan), eosin (TA01ES, BIOTnA Biotech, Taiwan), Martius scarlet blue (MSB; ScyTek, USA), and Oil Red O (TASS06, BIOTnA Biotech, Taiwan) staining kits were employed.

2.2 Blood clot analogue production system

A blood clot analogue production system was developed to replicate the hemodynamic conditions of arterial blood flow under continuous circulation. The system incorporated a pressure-controlled fluid network designed for long-term stable operation, with regulation of both flow rate and calcium concentration. This configuration enabled independent operation of each device; even during gradual clot formation, the flow rate in parallel devices remained unaffected.[27]

The overall system configuration is illustrated in Fig. 2A. A roller pump recirculated blood from the downstream to the upstream reservoirs, which were positioned on adjustable-height platforms. This arrangement allowed fine tuning of the hydrostatic pressure head, while calibrated flow-rate sensors (Fig. S1 and Table S2) ensured precise modulation of flow rate and shear stress. The upstream reservoir was gently agitated using a shaker module at 72 rpm to prevent sedimentation of blood cells, and the hydrostatic height difference between reservoirs generated the pressure driving blood through the tubing network. The network incorporated switching valves, hourglass-profiled fluidic channels, and flow-rate sensors, with real-time imaging of clot development provided using a digital microscope unit.

The system could be configured flexibly as either a single-loop (Fig. S2) or dual-loop recirculation network (Fig. 2B). In the dual-loop configuration, two independent loops, each consisting of paired upstream and downstream reservoirs linked to fluidic channels, could share the same blood source but operate in parallel under distinct flow or ionic conditions. This design enabled simultaneous experiments while reducing variability associated with biological differences.

An injection port in the upstream reservoir allowed controlled addition of $CaCl_2$ to initiate coagulation under defined ionic conditions. The time of injection was designated as time zero. A tubing switch permitted temporary flow interruption for sample retrieval or device adjustment.

2.3 Design, simulation, and fabrication of hourglass-profiled circular fluidic channels

The central component of the system was the hourglass-profiled circular fluidic channel, engineered to replicate the hemodynamic microenvironment of a stenosed artery under controlled flow conditions. Each channel featured a smoothly converging–diverging circular geometry. A tubing with a wall thickness of 0.5 mm and an inner diameter of 3.0 mm was used; accordingly, the fluidic channel incorporated regions with a diameter of 4.0 mm for tubing insertion, followed by a diameter gradient ranging from 3.0 mm at the inlet to 0.6

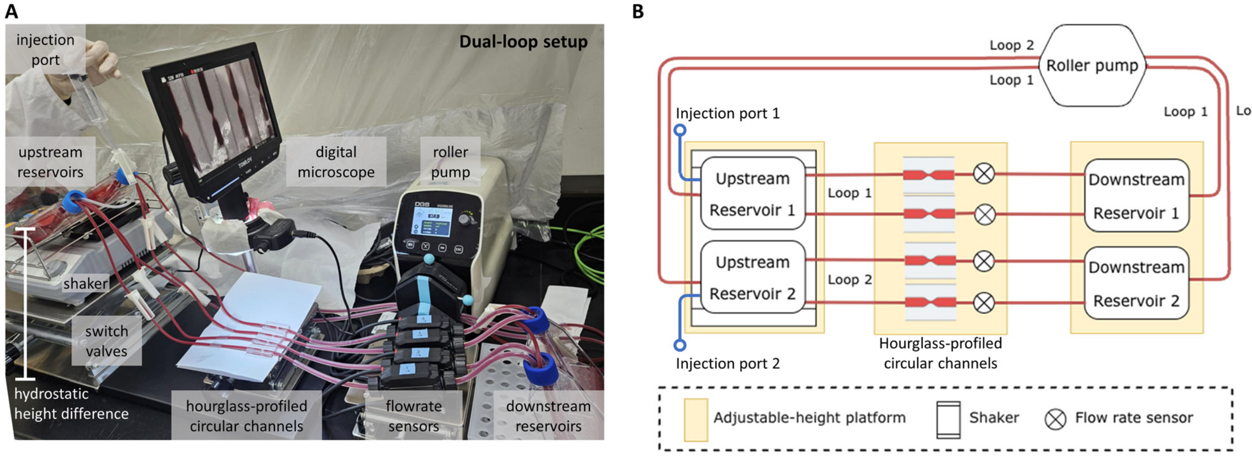

Fig. 2 Clot analogue production system. A) Photograph of the system. A roller pump recirculates blood from the downstream to the upstream reservoirs, which are mounted on adjustable-height platforms. The upstream reservoirs are gently agitated using a shaker module to reduce sedimentation of blood cells. The hydrostatic height difference between reservoirs generates the pressure driving blood through the tubing network, which includes switching valves, hourglass-profiled fluidic channels, and flow-rate sensors. Reagents can be introduced into the loop at any time *via* the injection port, and real-time imaging is provided using a digital microscope unit. B) Schematic diagram of the system, illustrating four hourglass-profiled circular channels that can operate in parallel to produce four clot analogues under two distinct experimental conditions, enabling flexible and comparative analyses.

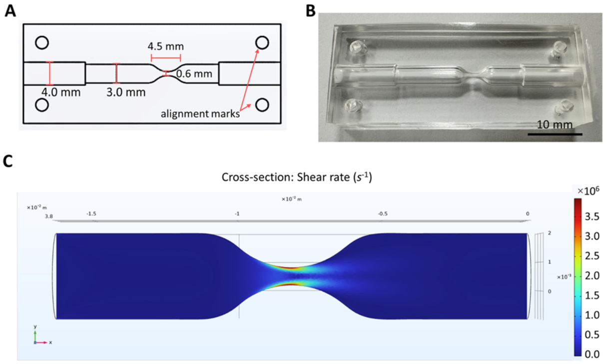

Fig. 3 Hourglass-profiled circular channel design and flow simulation. A) CAD drawing of the hourglass-profiled circular channel showing the converging–diverging geometry with a 3.0 mm inlet and a 0.6 mm constriction (20% of the inlet diameter), simulating severe arterial stenosis. B) Photograph of the PDMS device. C) Cross-sectional view of the CFD-simulated shear-rate distribution obtained using the k–ω turbulence model. The shear rate increased from approximately 10^4 s^{-1} at the inlet to over 10^6 s^{-1} at the constriction, then decreased downstream, reproducing the transition from stenotic to post-stenotic flow.

mm at the constriction (Fig. 3A and B), corresponding to 20% of the inlet diameter and representing severe arterial stenosis.

The hourglass geometry was optimized using computational fluid dynamics (CFD) simulations performed in COMSOL Multiphysics with the k–ω turbulence model. The analysis revealed a shear-rate gradient ranging from approximately 10^4 s^{-1} at the inlet, rising beyond 10^6 s^{-1} at the constriction wall, and decreasing again to $\sim 10^4$ s^{-1} downstream (Fig. 3C). These findings confirmed that the device could generate a localized high-shear region and reproduce the physiological transition from stenotic to post-stenotic flow, which could enable the controlled initiation and propagation of blood clot analogues under physiologically relevant flow conditions.

Fluidic channels were fabricated by casting PDMS twice from the same CNC-machined PMMA mold. Following a brief oxygen plasma treatment, the PDMS layers were aligned and bonded to form a circular channel with a central constriction.

2.4 Blood sample preparation and $CaCl_2$ concentration modulation

Prior to each experiment, a complete blood count (CBC) analysis was performed to verify hematological parameters and ensure consistency across different blood batches.

Before introducing blood, the clot analogue production system was filled with 1× phosphate-buffered saline (PBS) at a low flow rate (<5 mL min^{-1}, driven by a pressure head of 9.5 cm) to establish steady flow and remove trapped air bubbles. Porcine blood was then gradually infused, replacing the PBS buffer to achieve a stable low-flow baseline in a similar manner. Subsequently, the height difference between the upstream and downstream reservoirs was adjusted to 23 cm to achieve a target flow rate of ~20 mL min^{-1} per channel. The actual flow rate varied depending on the viscosity of the blood sample.

Coagulation was initiated by injecting a $CaCl_2$ solution into the circulating blood. The $CaCl_2$ concentration was varied between 1.8 and 16.5 mM (1.8, 2.3, 6.6, 12.6, and 16.5 mM) to examine the effect of calcium levels on clot formation kinetics and composition.

To evaluate the influence of calcium concentration on clot composition, the dual-loop clot analogue production system was operated under identical flow conditions but with different $CaCl_2$ concentrations. Both loops were supplied with the same batch of porcine blood, ensuring equivalent hematocrit and minimizing biological variability. Clot formation was monitored in real time using flow-rate sensors positioned downstream of each fluidic channel. A clot analogue was considered fully developed when the measured flow rate decreased to the sensor baseline (no-flow condition), indicating complete obstruction within the channel.

After perfusion, the fluidic channels were rinsed with PBS to remove residual blood, and the clot analogues were retrieved for histological analysis.

2.5 Clot analogue characterization and staining analysis

After perfusion, the PDMS fluidic channels were carefully disassembled, and clot analogues formed within the hourglass-profiled channels were gently retrieved using fine tweezers. The samples were immersed in PBS for 5 minutes, fixed in 4% paraformaldehyde (PFA) at 4 °C for 12 hours, and subsequently dehydrated and embedded in paraffin. Sections with a thickness of 3 μm were prepared for histological analysis.

For general structural characterization, sections were stained with hematoxylin and eosin (H&E) and Martius scarlet blue (MSB) to differentiate RBC-rich, fibrin–platelet, and leukocyte/neutrophil extracellular trap (NET)-rich regions. NET-rich regions were identified using a combination of color, structural characteristics, and spatial localization. Because NETs are composed of extracellular DNA and histones, they typically appeared as strands or smears with staining properties similar to nuclei and were consistently observed in association with leukocyte aggregates. Oil Red O staining was additionally performed to identify lipid components within the clot analogues.

Bright-field images of stained clot analogue sections were acquired under standardized illumination and exposure conditions, and quantitative analysis was performed. For H&E-stained sections, color separation was conducted in ImageJ/Fiji using the Colour Deconvolution plugin with the built-in H&E vector. For MSB-stained sections, color deconvolution followed the method of Ruifrok *et al.*, with stain vectors of each chromogenic component to match the spectral characteristics of the applied stains.[28] Following color separation, mean intensity values were calculated for each stain-specific channel derived from MSB staining, corresponding to erythrocyte-rich, fibrin-rich, and nucleus/NET-enriched regions. These values were used to represent the relative staining intensity of the respective clot analogue components.

3. Results and discussion

3.1 Clot analogue formation under controlled flow

Under continuous circulation, progressive clot formation was observed within the hourglass-profiled fluidic channel, typically initiating near the constriction region where local shear was the highest. The downstream flow-rate sensor recorded a gradual reduction in flow velocity corresponding to clot analogue growth, and the channel was considered fully occluded when the flow decreased to the sensor baseline.

Real-time flow-rate profiles are shown in Fig. 4. Stable flow conditions were typically established, followed by a sharp drop to baseline, indicating complete occlusion of the fluidic channel. With the exception of 2.3 mM $CaCl_2$, where all six flow-rate traces are displayed, and 1.8 mM $CaCl_2$, where only a single trace is shown, averaged flow-rate traces ($N = 2$) are presented for clarity, as replicate results were nearly identical. The occlusion time, defined as the point at which the flow rate reached half of its initial value, together with individual flow-rate traces from each blood sample, are provided in Fig. S3. Occlusion time decreased progressively with increasing $CaCl_2$ concentration (1.8–16.5 mM), underscoring the role of ionic calcium in modulating coagulation kinetics. At lower concentrations (1.8 and 2.3 mM $CaCl_2$), only about half of the devices exhibited occlusion within the perfusion period, which typically exceeded 300 min.

Comparisons between the fluidic channel and 3.0 mm diameter tubing configurations revealed distinct clot analogue formation behaviors. At higher $CaCl_2$ concentrations (6.6–16.5 mM), the tubing group reached occlusion more rapidly than the fluidic channel group. This difference suggested that the constricted geometry and associated high-shear region within the hourglass-profiled fluidic channel likely exerted an initial scouring effect, in which excessive shear ($>10^6$ s^{-1}) detached nascent aggregates and delayed the establishment of a stable clot analogue nucleus. In contrast, the straight-tube configuration, with a more uniform and moderate shear environment of approximately 10^4 s^{-1}, facilitated earlier platelet adhesion and continuous clot analogue growth.

At 2.3 mM $CaCl_2$, which approximates the concentration used in clinical blood transfusion preparations, the occlusion time varied considerably among replicates. Under this condition, no occlusion occurred in the tubing group. In the fluidic channel group, however, small, mobile aggregates were intermittently observed lodging and dislodging from the constriction region, as shown in Movies S1 and S2, indicating that clot formation was limited to transient, embolus-like fragments rather than stable occlusion.

These findings demonstrated that clot analogue formation was readily modulated by ionic calcium levels. At higher calcium concentrations, clot analogues formed rapidly and produced stable occlusion, whereas near-physiological calcium levels resulted in slow, shear-sensitive coagulation and the generation of transient, embolus-like aggregates.

3.2 Effect of $CaCl_2$ concentration on clot analogue formation and composition

For spatially resolved histological analysis, clot sections were subdivided according to the geometric features of the hourglass

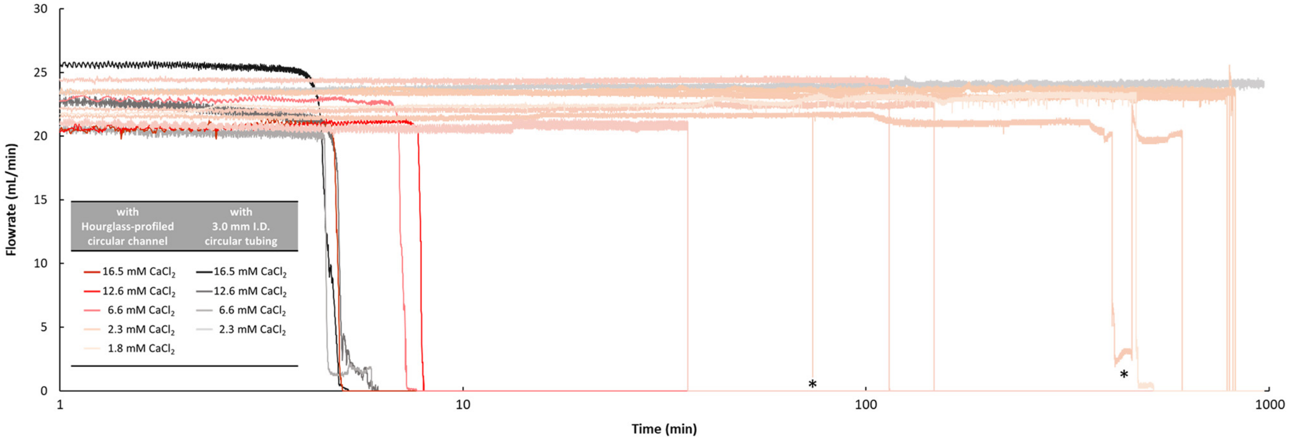

Fig. 4 Flow-rate profiles during clot analogue formation under various $CaCl_2$ concentrations using the dual-loop clot analogue production system. Real-time flow-rate traces were recorded by downstream sensors for $CaCl_2$ concentrations ranging from 1.8 to 16.5 mM. Data are shown as averaged traces ($N = 2$ for each concentration), except at 1.8 mM ($N = 1$) and 2.3 mM ($N = 6$, derived from four blood samples). Warm-colored curves represent experiments with the hourglass-profiled circular channel (1.8–16.5 mM $CaCl_2$), while grayscale curves represent experiments with 3.0 mm inner-diameter (I.D.) circular tubing (2.3–16.5 mM $CaCl_2$). In the hourglass-profiled channel, occlusion time increased progressively as $CaCl_2$ concentration decreased, indicating slower clot analogue development under reduced calcium ion conditions. At 2.3 mM, the $CaCl_2$ concentration typically used in clinical transfusion preparations, occlusion times were highly variable, and complete occlusion was not observed in the tubing group at or below this level. Asterisks ("*") denote the lodging and dislodging events of clot analogues at the constriction region shown in Movies S1 and S2. By contrast, at high $CaCl_2$ concentrations (6.6–16.5 mM), occlusion occurred more rapidly in the tubing than in the hourglass-profiled channel. Note the logarithmic scale on the *x*-axis. These results underscore the combined influence of calcium concentration and geometric confinement on coagulation dynamics.

channel. The narrowest segment, with a diameter smaller than 3.0 mm, was defined as the constriction region. The segment proximal to the constriction in the upstream flow direction was designated as the upstream region, while the segment distal to the constriction in the downstream flow direction was designated as the downstream region.

Clot analogues formed under different $CaCl_2$ concentrations (1.8–16.5 mM) exhibited distinct compositional and structural characteristics, as revealed by histological staining (Fig. 5). At high $CaCl_2$ concentrations (6.6–16.5 mM), clot analogues formed rapidly, typically within 10 minutes, and exhibited compact RBC–fibrin-dominated cores surrounded by thin platelet shells (Fig. 5F–H and K–M), morphologically resembling the laminar "Zahn line" structures characteristic of arterial-type thrombi.[29] At lower $CaCl_2$ concentrations (1.8 and 2.3 mM), the coagulation pathways were likely not activated initially, and the resulting clot analogues exhibited mechanically unstable structures with limited cohesion. Within the constricted region, small aggregates gradually merged into a loosely organized clot analogue, consistent with incomplete polymerization under low-calcium conditions. MSB staining revealed platelet–fibrin-rich regions with sparse RBC inclusion and occasional leukocyte/NET-positive zones near the periphery, indicating a shift toward a NET–platelet–fibrin composition (Fig. 5I and J).

3.3 Effect of shear rate on clot analogue formation and composition

Within the hourglass-profiled fluidic channel, regional variation along the upstream, constriction, and downstream regions influenced fibrin packing density. Fibrin fibers at the constriction appeared more tightly bundled and aligned compared with those in the upstream and downstream regions, consistent with the higher local shear rate that promotes fibrin elongation and compaction during polymerization. This spatial gradient suggests that geometric confinement and shear jointly modulate fibrin assembly, leading to region-dependent clot density and mechanical stability.

As shown in the constriction regions of Fig. 5H and M, fibrin fibers within the 6.6 mM $CaCl_2$ clots appeared highly condensed and interwoven, forming a laminar network that firmly encapsulated entrapped red blood cells. The downstream regions displayed more open fibrin bundles and larger interstitial spaces, reflecting the effect of decreased shear and local flow recirculation. The upstream region exhibited an intermediate morphology, with partially aligned fibrin strands surrounding RBC clusters. These spatial variations in fibrin density and orientation demonstrate that, even under identical ionic conditions, localized shear gradients modulate fibrin polymerization kinetics and fiber compaction.

Representative sections from the 6.6 mM $CaCl_2$ tubing group (Fig. 6A) showed loosely packed fibrin networks and fragmented platelet aggregates, consistent with reduced compaction in the absence of geometric constriction. In contrast, MSB staining of the corresponding fluidic channel clot analogue (Fig. 6B) revealed a compact organization consisting of a dense fibrin network and tightly packed erythrocytes, surrounded by a thin platelet-rich layer. This structure resembles the canonical arterial-type thrombus, in which the RBC–fibrin core provides mechanical rigidity while the platelet shell reinforces surface stability.

Notably, the peripheral NET-rich layer observed in the 6.6 mM $CaCl_2$ fluidic channel group was much less pronounced in the tubing samples (Fig. 6A and B), suggesting that high shear and local flow recirculation within the constricted geometry play critical roles in promoting neutrophil activation and NET release. Under higher shear conditions, platelet activation and degranulation can further stimulate neutrophils to extrude

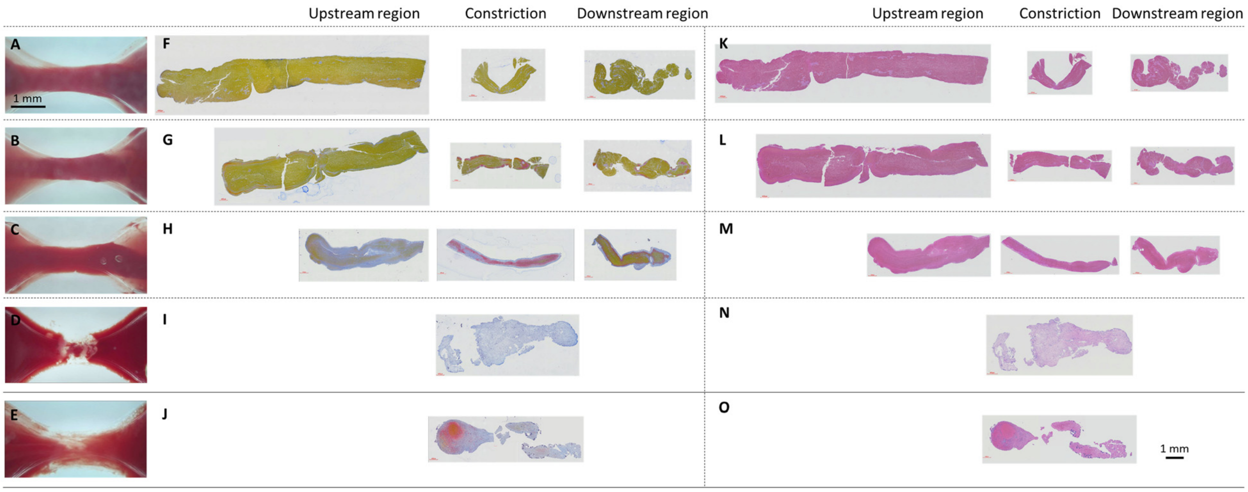

Fig. 5 Morphological and histological characterization of clot analogues formed under different $CaCl_2$ concentrations. Representative images show a single continuous clot analogue formed within the hourglass-profiled circular PDMS channel at five $CaCl_2$ concentrations: 16.5 mM, 12.6 mM, 6.6 mM, 2.3 mM and 1.8 mM. A–E) In-channel clot analogues prior to retrieval; F–J) Martius scarlet blue (MSB) staining and K–O) hematoxylin and eosin (H&E) staining of upstream, constriction, and downstream regions. Clot analogues formed at 2.3 mM and 1.8 mM $CaCl_2$ were loosely structured and easily separated into segments. A–E are shown in the same magnification and F–O are also shown at the same magnification.

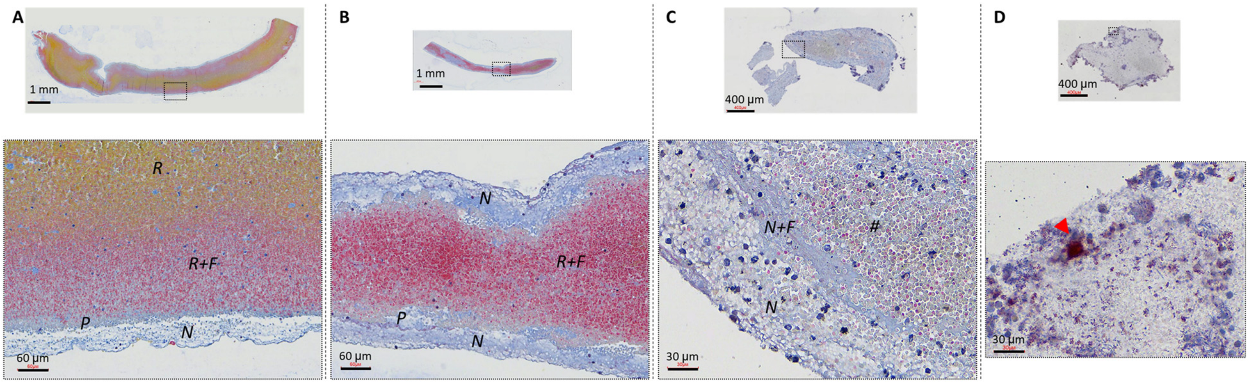

Fig. 6 Morphological and histological characterization of representative clot analogues formed under different shear rates and $CaCl_2$ concentrations. MSB staining of clot analogues formed with 6.6 mM $CaCl_2$: A) inside the 3.0 mm I.D. tubing and B) in the hourglass-profiled circular channel. The clot formed in the tubing displayed looser layers and a distinct RBC-dominant core (*R*). In contrast, the clot analogue formed around the constricted region exhibited a concentric structure composed of an outer neutrophil extracellular trap (NET)-rich shell (*N*), a platelet-rich zone (*P*), and an inner RBC–fibrin-rich core (*R* + *F*) consisting of densely packed erythrocytes interwoven with compact fibrin fibers. C) The clot analogue formed at 1.8 mM $CaCl_2$ showed a peripheral NET-rich shell (*N*), followed by a NET–fibrin zone (*N* + *F*), and an inner platelet–fibrin matrix with sparse RBC inclusion (*#*). D) Oil Red O staining of a clot analogue formed at 2.3 mM $CaCl_2$ revealed a lipid-rich zone (arrowhead) within the peripheral NET-rich region.

chromatin networks that intertwine with fibrin, forming the outer NET–platelet–fibrin shell characteristic of arterial-type thrombi.

At reduced calcium levels, such as 1.8 mM $CaCl_2$, clot analogues generated in the fluidic channel exhibited a more diffuse NET–platelet–fibrin architecture (Fig. 6C), indicating that under low-calcium conditions, clot analogue formation is primarily governed by platelet–neutrophil inflammatory crosstalk rather than fibrin polymerization. These diffuse, NET-rich architectures, composed of platelet–fibrin–DNA networks with sparse RBC inclusion, may recapitulate the inflammatory, hypocalcemic clot phenotype frequently described in stroke specimens.[30–32] A similar structural pattern was observed in the 2.3 mM $CaCl_2$ group (Fig. 6D), reinforcing that even in hypocalcemic environments, inflammatory activation can substitute for classical fibrin crosslinking to stabilize the clot framework.

Although fibrin was still detectable within NET-rich regions under low-Ca^{2+} conditions, its distribution appeared sparse and discontinuous, suggesting that fibrin formation occurred secondary to NET scaffold development rather than being the primary driver of clot assembly.

Oil red O staining (Fig. 6D) revealed lipid accumulation within the peripheral NET-rich region, indicating the coexistence of membrane-derived vesicles and extracellular chromatin networks. This suggests that the NET–platelet–fibrin scaffold can entrap lipid components under low-calcium, high-shear conditions, further contributing to the loose and heterogeneous morphology of the clot.

To quantitatively compare the major components of the clot analogues, image analysis was performed on chromogen-specific colors from MSB-stained sections. As shown in Fig. 7, the percentage of RBCs increased with increasing $CaCl_2$ concentration, while the proportion of nuclei/NET decreased. At 6.6 mM $CaCl_2$, the in-tube clot analogues contained higher percentages of RBCs and fibrin compared with those formed in the hourglass-profiled channel.

Collectively, these observations reveal a continuum in clot architecture: from compact, RBC–fibrin-dominated thrombus-like analogues formed under high-calcium, high-shear conditions to loose, NET–fibrin-rich networks generated under low-calcium environments. This demonstrates that clot analogue morphology can be tuned within the same fluidic system by adjusting calcium ion concentration and shear conditions.

3.4 Clot analogue retrievability and translational relevance of the PDMS fluidic channel

The PDMS fluidic channel enabled the formation of elongated clot analogues along the constricted region under continuous flow for more than 1000 minutes, if desired. Upon termination of perfusion, clot analogues could be readily retrieved using fine

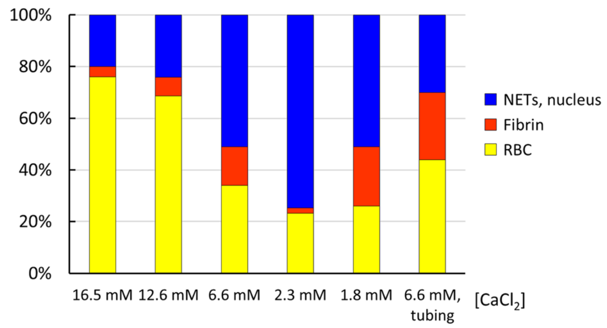

Fig. 7 Quantification of clot analogue composition. Image analysis of MSB-stained sections was used to compare major clot components. The percentage of RBCs increased with higher $CaCl_2$ concentrations, while nuclei/NETs decreased. At 6.6 mM $CaCl_2$, in-tube clot analogues contained greater proportions of RBCs and fibrin compared with those formed in the hourglass-profiled channel (*N* = 1).

tweezers (Fig. S4). The harvested clot analogues remained structurally intact, without rupture or deformation, as confirmed by histological staining.

This straightforward retrieval capability allows the direct use of clot analogues for subsequent mechanical thrombectomy testing, including aspiration and stent-retriever procedures. By integrating parallel clot analogue production and harvesting, the system provides a reproducible and physiologically relevant platform to study clot-device interactions.

Importantly, the platform adheres to the ethical 3R principles (Replacement, Reduction, and Refinement) by replacing animal-based thrombosis models with a fully *in vitro* system, reducing animal usage through repeated trials from a single blood batch, and refining experimental control over biochemical and hemodynamic parameters.[33,34]

3.5 Clinical relevance and compositional heterogeneity

The PDMS hourglass-profiled fluidic channel enables precise and reproducible modulation of clot analogue composition by simultaneously controlling calcium ion concentration and flow shear conditions. By tuning $CaCl_2$ levels from 1.8 mM to 16.5 mM, the system can generate clot analogues with distinct phenotypes, ranging from RBC–fibrin-dominated to platelet–NET–fibrin-enriched architectures, thus recapitulating the compositional heterogeneity observed in patient-derived thrombi.

Clinical histopathological analyses have demonstrated that ischemic stroke thrombi are highly heterogeneous in both composition and structure. In a systematic study of 177 retrieved clots, two principal domains, RBC-rich and platelet-rich zones, were identified as interwoven within the same thrombus.[9] The platelet-rich regions consisted of dense fibrin-von Willebrand factor (vWF) scaffolds enriched with leukocytes and extracellular DNA, while the RBC-rich areas contained compact erythrocyte aggregates embedded within thin fibrin strands. NETs were predominantly localized at the interfaces between these domains, forming DNA–platelet–fibrin hybrid layers that confer resistance to both recombinant tissue plasminogen activator (rt-PA)-mediated thrombolysis and mechanical thrombectomy.

These clinical findings indicate that the biochemical and structural heterogeneity of thrombi governs their mechanical stability and therapeutic responsiveness. Our *in vitro* clot analogue production system provides a controllable platform to systematically reproduce these heterogeneous architectures, enabling direct investigation of how clot composition, shear environment, and ionic milieu influence thrombus maturation and treatment outcomes.

3.6 Shear gradients as mechanistic drivers of thrombus stratification

Shear forces are recognized as key determinants of thrombus architecture.[35] Under physiological arterial flow (10^4–10^5 s^{-1}), high shear promotes platelet adhesion and fibrin compaction, resulting in mechanically robust RBC–fibrin cores.[36] Conversely, localized shear gradients and recirculation zones stimulate platelet–neutrophil interactions and NET formation, particularly when coagulation is partially inhibited.[37] Nesbitt *et al.*[38] further demonstrated that thrombus formation is driven by microgradients of shear, where alternating acceleration and deceleration zones induce platelet aggregation independent of soluble agonists.

These findings align with the observed behavior in the hourglass-profiled circular fluidic channel, where the constricted region reproduces high-shear acceleration, and the downstream expansion generates localized recirculation. Together, these dynamics promote the formation of distinct clot analogue architectures under various calcium concentrations and shear regimes.

3.7 Implications and future applications

By integrating chemical and hemodynamic control, this clot analogue production system bridges the gap between clinical pathology and mechanistic experimentation. The ability to precisely tune Ca^{2+} concentration and shear profiles enables the reproducible generation of both RBC–fibrin-rich and NET-rich clot analogues, providing a physiologically relevant *in vitro* model for investigating clot stability, fibrinolytic resistance, and device-clot interactions.

In particular, the dual-loop configuration allows multiple clot fluidic channels to operate simultaneously under distinct hemodynamic and biochemical conditions using the same blood batch, eliminating donor variability and enabling direct side-by-side comparison of clot phenotypes. This parallel design provides an efficient framework to study how subtle changes in calcium levels or shear gradients dictate thrombus composition and mechanics within a single run. Future studies may explore surface modification, tissue culture integration, and diverse channel constriction profiles to establish more specific, biomimetic environments for advancing our understanding of thrombotic processes.

This clot analogue production system offers a reusable, closed-loop platform that reduces animal use, avoids whole-animal procedures, and refines experimental variability through standardized geometry and flow conditions. Beyond thrombectomy simulation, it enables precise evaluation of fibrinolytic therapies, anti-NET interventions, and device performance across heterogeneous clot phenotypes. Ultimately, it provides a unified mechanistic and translational framework to guide the design of more effective thrombolytic and interventional strategies.

4. Conclusions

This study demonstrates that calcium ion concentration and local hemodynamic shear are decisive regulators of clot analogue phenotype. Using the hourglass-profiled circular PDMS fluidic channel, we reproduced the full spectrum of clot morphologies observed clinically—from compact, RBC–fibrin-dominated cores to loosely structured, NET-enriched networks—within a controllable *in vitro* environment. The dual-loop configuration further enables parallel clot formation under distinct conditions from the same blood source, minimizing variability and allowing direct comparison of phenotypes. Overall, this platform provides a physiologically relevant and reproducible framework for investigating clot maturation, fibrinolytic resistance, and thrombectomy device performance, thereby supporting the rational design of next-generation thrombolytic and interventional strategies.

Author contributions

Chun-Hsin Hsu: conceptualization, methodology, investigation, validation, writing – original draft, and project administration. To-Wen Chen: conceptualization, methodology, investigation, and validation. Wei-Jen Soong: methodology, investigation, and validation. Chihchen Chen: conceptualization, project administration, investigation, and writing – review & editing.

Conflicts of interest

The authors declare no conflicts of interest.

Data availability

All data associated with this study are present in the paper or the supplementary information (SI). Raw data that support the findings of this study are available from the corresponding author, C. C. upon reasonable request.

Supplementary information is available. See DOI: https://doi.org/10.1039/d6lc00190d.

Acknowledgements

This research was supported by the National Science and Technology Council (NSTC) of Taiwan under grant numbers 112-2223-E-007-014, 113-2223-E-007-017, and 114-2221-E-007-098. The authors gratefully acknowledge Dr. Albert J. Shih for his valuable guidance on the formation of blood clot analogues. We also thank the National Center for Instrumentation Research, the National Institutes of Applied Research, and the Agricultural Technology Research Institute for providing porcine blood samples.

References

1 R. Lozano, M. Naghavi, K. Foreman, S. Lim, K. Shibuya, V. Aboyans, J. Abraham, T. Adair, R. Aggarwal, S. Y. Ahn, M. Alvarado, H. R. Anderson, L. M. Anderson, K. G. Andrews, C. Atkinson, L. M. Baddour, S. Barker-Collo, D. H. Bartels, M. L. Bell, E. J. Benjamin, D. Bennett, K. Bhalla, B. Bikbov, A. Bin Abdulhak, G. Birbeck, F. Blyth, I. Bolliger, S. Boufous, C. Bucello, M. Burch, P. Burney, J. Carapetis, H. Chen, D. Chou, S. S. Chugh, L. E. Coffeng, S. D. Colan, S. Colquhoun, K. E. Colson, J. Condon, M. D. Connor, L. T. Cooper, M. Corriere, M. Cortinovis, K. C. de Vaccaro, W. Couser, B. C. Cowie, M. H. Criqui, M. Cross, K. C. Dabhadkar, N. Dahodwala, D. De Leo, L. Degenhardt, A. Delossantos, J. Denenberg, D. C. Des Jarlais, S. D. Dharmaratne, E. R. Dorsey, T. Driscoll, H. Duber, B. Ebel, P. J. Erwin, P. Espindola, M. Ezzati, V. Feigin, A. D. Flaxman, M. H. Forouzanfar, F. G. Fowkes, R. Franklin, M. Fransen, M. K. Freeman, S. E. Gabriel, E. Gakidou, F. Gaspari, R. F. Gillum, D. Gonzalez-Medina, Y. A. Halasa, D. Haring, J. E. Harrison, R. Havmoeller, R. J. Hay, B. Hoen, P. J. Hotez, D. Hoy, K. H. Jacobsen, S. L. James, R. Jasrasaria, S. Jayaraman, N. Johns, G. Karthikeyan, N. Kassebaum, A. Keren, J. P. Khoo, L. M. Knowlton, O. Kobusingye, A. Koranteng, R. Krishnamurthi, M. Lipnick, S. E. Lipshultz, S. L. Ohno, J. Mabweijano, M. F. MacIntyre, L. Mallinger, L. March, G. B. Marks, R. Marks, A. Matsumori, R. Matzopoulos, B. M. Mayosi, J. H. McAnulty, M. M. McDermott, J. McGrath, G. A. Mensah, T. R. Merriman, C. Michaud, M. Miller, T. R. Miller, C. Mock, A. O. Mocumbi, A. A. Mokdad, A. Moran, K. Mulholland, M. N. Nair, L. Naldi, K. M. Narayan, K. Nasseri, P. Norman, M. O'Donnell, S. B. Omer, K. Ortblad, R. Osborne, D. Ozgediz, B. Pahari, J. D. Pandian, A. P. Rivero, R. P. Padilla, F. Perez-Ruiz, N. Perico, D. Phillips, K. Pierce, C. A. Pope, 3rd, E. Porrini, F. Pourmalek, M. Raju, D. Ranganathan, J. T. Rehm, D. B. Rein, G. Remuzzi, F. P. Rivara, T. Roberts, F. R. De Leon, L. C. Rosenfeld, L. Rushton, R. L. Sacco, J. A. Salomon, U. Sampson, E. Sanman, D. C. Schwebel, M. Segui-Gomez, D. S. Shepard, D. Singh, J. Singleton, K. Sliwa, E. Smith, A. Steer, J. A. Taylor, B. Thomas, I. M. Tleyjeh, J. A. Towbin, T. Truelsen, E. A. Undurraga, N. Venketasubramanian, L. Vijayakumar, T. Vos, G. R. Wagner, M. Wang, W. Wang, K. Watt, M. A. Weinstock, R. Weintraub, J. D. Wilkinson, A. D. Woolf, S. Wulf, P. H. Yeh, P. Yip, A. Zabetian, Z. J. Zheng, A. D. Lopez, C. J. Murray, M. A. AlMazroa and Z. A. Memish, *Lancet*, 2012, **380**, 2095–2128.

2 A. M. Wendelboe and G. E. Raskob, *Circ. Res.*, 2016, **118**, 1340–1347.

3 World Health Organization, The top 10 causes of death, https://www.who.int/news-room/fact-sheets/detail/the-top-10-causes-of-death, (accessed 7 August 2024).

4 G. Alkarithi, C. Duval, Y. Shi, F. L. Macrae and R. A. S. Ariens, *Arterioscler., Thromb., Vasc. Biol.*, 2021, **41**, 2370–2383.

5 J. L. Carson, M. A. Kelley, A. Duff, J. G. Weg, W. J. Fulkerson, H. I. Palevsky, J. S. Schwartz, B. T. Thompson, J. Popovich, T. E. Hobbins, M. A. Spera, A. Alavi and M. L. Terrin, *N. Engl. J. Med.*, 1992, **326**, 1240–1245.

6 S. Bracard, X. Ducrocq and J. L. Mas, *Lancet Neurol.*, 2016, **15**, 1203.

7 A. P. Jadhav, S. M. Desai and T. G. Jovin, *Neurology*, 2021, **97**, S126–S136.

8 K. Suzuki, Y. Matsumaru and M. Takeuchi, *JAMA, J. Am. Med. Assoc.*, 2021, **325**, 1795.

9 S. Staessens, F. Denorme, O. François, L. Desender, T. Dewaele, P. Vanacker, H. Deckmyn, K. Vanhoorelbeke, T. Andersson and S. F. De Meyer, *Haematologica*, 2020, **105**, 498–507.

10 A. Bhambri, A. R. Adapa, Y. Liu, T. Boeckh-Behrens, V. Procházka, F. Hernández-Fernández, R. A. Barbella-Aponte, T. Hashimoto, L. E. Savastano, J. J. Gemmete, N. Chaudhary, A. J. Shih and A. S. Pandey, *Neurosurgery*, 2021, **89**, 1122–1131.

11 S. H. Xu, Z. Y. Yang, J. Y. Jia, S. J. Zhang, S. M. Huang, L. Zhang, M. Guan, G. B. Chen, X. Y. Leng and L. A. Huang, *J. Am. Heart Assoc.*, 2025, **14**, e039199.

12 L. Di Meglio, J. P. Desilles, V. Ollivier, M. S. Nomenjanahary, S. Di Meglio, C. Deschildre, S. Loyau, J. M. Olivot, R. Blanc, M. Piotin, M. C. Bouton, J. B. Michel, M. Jandrot-Perrus, B. Ho-Tin-Noé and M. Mazighi, *Neurology*, 2019, **93**, E1686–E1698.

13 E. Dohle, A. H. Ashok, S. Bhakta, I. Induruwa and N. R. Evans, *J. Thromb. Thrombolysis*, 2025, **58**, 355–369.

14 A. Aliena-Valero, J. Baixauli-Martin, G. Torregrosa, J. I. Tembl and J. B. Salom, *J. Stroke*, 2021, **23**, 327–342.

15 Y. Liu, A. S. Reddy, J. Cockrum, M. C. Ajulufoh, Y. Zheng, A. J. Shih, A. S. Pandey and L. E. Savastano, *J. Stroke Cerebrovasc. Dis.*, 2020, **29**, 105205.

16 D. A. Kim and D. N. Ku, *Blood Adv.*, 2022, **6**, 2872–2883.

17 T. C. Merkel, V. I. Bondar, K. Nagai, B. D. Freeman and I. Pinnau, *J. Polym. Sci.*, 2000, **38**, 415–434.

18 E. Berthier, E. W. K. Young and D. Beebe, *Lab Chip*, 2012, **12**, 1224–1237.

19 I. Miranda, A. Souza, P. Sousa, J. Ribeiro, E. M. S. Castanheira, R. Lima and G. Minas, *J. Funct. Biomater.*, 2022, **13**, 2.

20 F. J. Tovar-Lopez, G. Rosengarten, E. Westein, K. Khoshmanesh, S. P. Jackson, A. Mitchell and W. S. Nesbitt, *Lab Chip*, 2010, **10**, 3427.

21 B. Ramaswamy, Y. T. T. Yeh and S. Y. Zheng, *Sens. Actuators, B*, 2013, **180**, 21–27.

22 J. Berry, F. J. Peaudecerf, N. A. Masters, K. B. Neeves, R. E. Goldstein and M. T. Harper, *Lab Chip*, 2021, **21**, 4104–4117.

23 H. Deal, E. M. Byrnes, S. Pandit, A. Sheridan, A. C. Brown and M. Daniele, *Lab Chip*, 2025, **25**, 440–453.

24 C. Q. Yao, Z. Y. Dong, Y. C. Zhang, Y. Mi, Y. C. Zhao and G. W. Chen, *AIChE J.*, 2015, **61**, 3964–3972.

25 P. M. Korczyk, V. van Steijn, S. Blonski, D. Zaremba, D. A. Beattie and P. Garstecki, *Nat. Commun.*, 2019, **10**, 2528.

26 W. M. S. Russell and R. L. Burch, *The principles of humane experimental technique*, Methuen, London, 1959.

27 K. M. Shen, K. Morikawa, T. Kitamori and C. Chen, *Chem. Eng. Sci.*, 2025, **304**, 121078.

28 A. C. Ruifrok and D. A. Johnston, *Anal. Quant. Cytol.*, 2001, **23**, 291–299.

29 R. Lee, D. Adlam, C. A. Clelland and K. M. Channon, *Eur. Heart J.*, 2012, **33**, 1039–1039.

30 E. Laridan, F. Denorme, L. Desender, O. François, T. Andersson, H. Deckmyn, K. Vanhoorelbeke and S. F. De Meyer, *Ann. Neurol.*, 2017, **82**, 223–232.

31 C. Ducroux, L. Di Meglio, S. Loyau, S. Delbosc, W. Boisseau, C. Deschildre, M. Ben Maacha, R. Blanc, H. Redjem, G. Ciccio, S. Smajda, R. Fahed, J. B. Michel, M. Piotin, L. Salomon, M. Mazighi, B. Ho-Tin-Noe and J. P. Desilles, *Stroke*, 2018, **49**, 754–757.

32 L. L. Swystun and P. C. Liaw, *Blood*, 2016, **128**, 753–762.

33 J. M. Clark, *Br. J. Nutr.*, 2018, **120**, S1–S7.

34 J. Ranjbar, J. M. Gibbins, J. Roe, P. Roach, Y. Yang and A. G. S. Harper, *F1000Research*, 2025, **14**, 110.

35 S. P. Jackson, *Nat. Med.*, 2011, **17**, 1423–1436.

36 L. D. C. Casa, D. H. Deaton and D. N. Ku, *J. Vasc. Surg.*, 2015, **61**, 1068–1080.

37 J. Li, K. Kim, A. Barazia, A. Tseng and J. Cho, *Cell. Mol. Life Sci.*, 2015, **72**, 2627–2643.

38 W. S. Nesbitt, E. Westein, F. J. Tovar-Lopez, E. Tolouei, A. Mitchell, J. Fu, J. Carberry, A. Fouras and S. P. Jackson, *Nat. Med.*, 2009, **15**, 665–673.